Scientific Reports https://doi.org/10.1038/s41598-026-37736-z

Article in Press

Electronically switchable dual-band capsule antenna for wireless endoscopic applications

Received: 7 November 2025

Accepted: 23 January 2026

Published online: 27 January 2026

Cite this article as: Gogosh N., Khalid S., Malik B.T. *et al.* Electronically switchable dual-band capsule antenna for wireless endoscopic applications. *Sci Rep* (2026). https://doi.org/10.1038/s41598-026-37736-z

Nayab Gogosh, Sohail Khalid, Bilal Tariq Malik, M. Farhan Shafique, Stanislaw Szczepanski & Slawomir Koziel

We are providing an unedited version of this manuscript to give early access to its findings. Before final publication, the manuscript will undergo further editing. Please note there may be errors present which affect the content, and all legal disclaimers apply.

If this paper is publishing under a Transparent Peer Review model then Peer Review reports will publish with the final article.

ARTICLE IN PRESS

© The Author(s) 2026. **Open Access** This article is licensed under a Creative Commons Attribution-NonCommercial-NoDerivatives 4.0 International License, which permits any non-commercial use, sharing, distribution and reproduction in any medium or format, as long as you give appropriate credit to the original author(s) and the source, provide a link to the Creative Commons licence, and indicate if you modified the licensed material. You do not have permission under this licence to share adapted material derived from this article or parts of it. The images or other third party material in this article are included in the article's Creative Commons licence, unless indicated otherwise in a credit line to the material. If material is not included in the article's Creative Commons licence and your intended use is not permitted by statutory regulation or exceeds the permitted use, you will need to obtain permission directly from the copyright holder. To view a copy of this licence, visit http://creativecommons.org/licenses/by-nc-nd/4.0/.

Electronically Switchable Dual-Band Capsule Antenna for Wireless Endoscopic Applications

Nayab Gogosh[1,2], Sohail Khalid[3], Bilal Tariq Malik[2,] M. Farhan Shafique[2], Stanislaw Szczepanski[4] and Slawomir Koziel[*,4,5]

[1]Electrical and Computer Engineering Department, Riphah International University, Islamabad, Pakistan.

[2]Electrical Engineering Department, COMSATS University Islamabad, Park Road, Islamabad, Pakistan.

[3]Department of Computer Science, University of Management and Technology, Lahore, Pakistan.

[4]Faculty of Electronics, Telecommunications, and Informatics, Gdansk University of Technology, 80-233 Gdansk, Poland.

[5]Engineering Optimization and Modeling Center, Reykjavik University, 101 Reykjavik, Iceland.

[*]koziel@ru.is

ABSTRACT

This paper presents a highly compact linearly polarized planar dual annular ring antenna designed for wireless capsule endoscopy. The focus of this work on the small intestine is motivated by clinical practice in capsule endoscopy. Most capsule endoscopy systems are specifically designed to examine the small intestines, which are difficult to access with conventional wired endoscopes and are the primary region of interest for many gastrointestinal pathologists. The antenna is derived from a conventional annular ring structure and supports dual-band operation, covering both Wi-Fi frequencies at 2.45 GHz and 5.8 GHz. With a radius of only 4.7 mm, the planar geometry occupies minimal space inside the capsule, leaving more room for essential electronics and the battery. The antenna achieves bandwidths of 20.8 % at the lower band and 6.7 % at the upper band. A key feature of the design is the capability for electronic switching of the higher band, which enables efficient power management. This allows continuous transmission of critical data, such as control signals, over the lower band, while high-volume data, such as images and video, can be transmitted on demand over the upper band through microcontroller-controlled switching. This mechanism ensures battery conservation as well as reduced time average SAR levels for higher safety. In-vitro testing of the prototypes was conducted, and the measured gains of -17.3 dBi and -18 dBi at the lower and upper bands have been achieved. Furthermore, the antenna exhibits specific absorption rate (SAR) values of 21.5 W/kg and 24.7 W/kg for the two operating bands. To ensure safe operation in compliance with IEEE and ECC standards, maximum transmit powers of 93 mW and 81 mW can be utilized, respectively, while maintaining reliable link quality and extended communication coverage. The link margin remains at 21.1 dB and 12.3 dB at 2.45 GHz and 5.8 GHz, respectively, ensuring an excellent link reliability at a distance of 4 m.

Keywords

Biomedical telemetry, dual-band antenna, ingestible antenna, switchable antenna

Introduction

Biomedical telemetric systems enable the continuous acquisition and transmission of physiological data from the human body. Conventionally, this has been achieved using wearable sensors and antennas that enable a wide range of personal healthcare and remote monitoring applications[1-3]. These body-centric devices benefit from the ease of deployment and reusability, and relaxed size constraints compared to implanted systems.

However, certain diagnostic procedures require access to deeper internal tissues where external sensors cannot capture information. For such cases, ingestible capsule-based diagnosis systems have emerged as a minimally invasive solution in which a compact self-contained electronic pill travels naturally through the digestive tract while capturing and relaying medical imagery and associated sensor data [4, 5]. These ingestible antennas must operate in a highly constrained environment, facing significant design and performance challenges such as high tissue absorption, miniaturization, and strict compliance with the radiation exposure limits [6].

Recent advances in ultra-low power microcontrollers and compact RF front ends have made it possible for biomedical devices to function as standalone IoT nodes. With dual-band Wi-Fi radios now available in extremely small form factors, an ingestible capsule can communicate directly with standard access points without the need for a dedicated gateway. This capability opens the door to lower-cost remote healthcare where patients can be monitored seamlessly outside a clinical setting.

In the future, swallowable capsules are expected to become part of the routine home-based screening process. A patient could simply ingest the capsule, and the captured images would be transmitted in real time over Wi-Fi to a remote monitoring station where specialists would have access to diagnostic data. Achieving such flexibility requires a compact antenna solution that can support reliable communication at both 2.45 GHz and 5.8 GHz ISM bands, which are also shared with Wi-Fi physical layer standards. A dual-band usage would, however, increase the time-average SAR exposure [7, 8].

The existing literature mainly comprises antennas that are built on a flexible substrate, and later rolled inside the capsule along the inner edge [9-14]. This is a useful approach; however, it covers most of the side wall of the capsule, and hence the camera has a limited field of view, particularly to the front only. Secondly, the associated electronics are also enclosed inside the wrapped antenna; therefore, there is an issue of electromagnetic interference. On the other hand, planar antennas offer better utilization of the precious space inside the capsule but struggle with lower efficiency and elevated SAR levels. For example, a 6 mm diameter circular planar antenna using E and L-shaped slots achieves a gain of -20.8 dBi and exhibits a high SAR of 30.2 W/kg [15]. A dual-band square planar antenna design, reported in [16], achieves a gain of -28.2 dBi and -24.5 dBi for 915 MHz and 2.45 GHz bands. The antenna has a size of 6.5 mm × 6.5 mm and offers a bandwidth of 13.6 % and 6.28 % for the two resonant bands, respectively.

A circular disc antenna with a resonant frequency of 2.45 GHz was proposed, which has a diameter of 10.4 mm. The antenna covers a narrow bandwidth of 3.9 % and produces a low gain of -26.4 dBi [17]. Another work reports on a circular disc antenna that operates on a single frequency of 2.45 GHz and has a diameter of 9.8 mm. The antenna offers a bandwidth of 6 % and a high SAR level of 45.5 W/kg. High SAR restricts the transmit power level to only 44 mW [18]. A more recent square patch dual-band design of 8.2 mm × 8.2 mm also reports a low realized gain of -29.4 dBi and -30.3 dBi and bandwidths of 7.2 % and 4.2 % for 1.4 GHz and 2.45 GHz bands, respectively [19].

Overall, the literature indicates that while planar antennas offer practical integration advantages, their low gain and high SAR remain a significant challenge, particularly when aiming for longer link range, like in the case of Wi-Fi connectivity. This work intends to address these limitations, along with a switchable mechanism of a higher band to reduce the time-averaged exposure to the human body, as well as the conservation of the onboard battery.

The paper is organized as follows: Section II details the antenna specification. The evolution of the antenna is presented in Section III. Biocompatibility and SAR analysis of the antenna are discussed in Section IV. Electronic switching of the higher band is reported in Section V. Fabrication, measurement, and discussion for the single band, double band, and switchable antenna results are presented in Section VI. Section VII concludes the study.

Antenna specifications

WiFi 6 connectivity operates as a dual-band system extending earlier Wi-Fi standards that predominantly used the 2.45 GHz band. Dual-band capability is particularly important for future capsule endoscopy applications. The 5.8 GHz band supports higher data rates and is therefore suitable for transmitting bandwidth-intensive information such as video frames and images, whereas the 2.45 GHz band provides superior penetration and coverage, making it ideal for lower-rate telemetry and control signals. Importantly, both 2.45 GHz and 5.8 GHz Wi-Fi bands lie within the globally available ISM spectrum used by medical telemetry devices. This allows the upper OSI layers' communication protocols (MAC and network layers) to adopt the standard IEEE 802.11 functionalities, enabling the capsule to operate as an independent IoT node capable of direct IP connectivity without relying on a dedicated external gateway.

Since the capsule's battery must last throughout the duration of testing, power optimization is a critical consideration. An effective solution is to design an antenna that primarily operates at 2.45 GHz but can turn ON the 5.8 GHz band on demand, thus conserving the battery power for extended usage. Secondly, this switching mechanism will also reduce the time-averaged SAR exposure to human tissues by switching OFF the higher band when not in use, thereby enhancing the overall safety compliance.

This strategy balances performance, regulatory requirements, and energy efficiency, ultimately extending battery life while maintaining data integrity and human safety.

Antenna design

A circular disk antenna is the preferred choice for a planar topology because of the cylindrical geometry of the endoscopic capsule. A substrate with a higher permittivity is preferable to reduce the physical size of the antenna. A traditional circular patch antenna served as the basis for the proposed antenna design. The Rogers 3010 laminate substrate, which has a dielectric loss tangent of 0.0035 and a relative permittivity of 10.2, was utilized for the design. The resonant modes supported by circular microstrip antennas are inherently transverse magnetic in nature (TM_{nm}) owing to the presence of the ground plane underneath that enforces the Electric field to have a z-component. Consequently, the magnetic fields have no H_z component and are entirely transverse to the direction of propagation (z-axis). The fundamental mode of operation for a circular patch antenna is TM_{11}. Based on the mathematical relation, the diameter of a circular patch antenna should be approximately 22.4 mm to achieve the resonant frequency of 2.45 GHz [20]. However, the substrate size must be limited to 9.5 mm in order to fit within a capsule having an inner radius of 10 mm.

One of the potential solutions is to use an annular ring antenna instead of employing a solid patch antenna. An annular ring antenna is the modified version of a circular patch in which the middle section is free of metal, and a ring of copper is used for radiation at the periphery of the substrate. This arrangement allows for manipulating the fields in a better way and also enables the possibility of generating multiple resonances. A basic annular ring was created as a starting design that was fed from the center of the substrate through a microstrip section. The fundamental mode in the annular ring antenna is TM_{11} mode, similar to a circular patch antenna, the relation to calculate the resonant frequency of a particular TM mode is presented in (1)

$$f_{nm} = \frac{ck_{nm}}{2\pi\sqrt{\varepsilon_r}} \tag{1}$$

Where, k_{nm} is calculated through the derivatives of the Bessel and Neumann functions [21].

The equation (1) can be approximated as (2) [22]

$$f_{nm} = \frac{c}{2\pi\sqrt{\varepsilon_r}} \bullet \frac{X'_{nm}}{(a+b)/2} \tag{2}$$

Where a is the outer radius of the ring, b is the inner radius of the annular ring, X'_{nm} is the effective root calculated from annular ring boundary conditions. The value of X'_{nm} for TM_{11} mode is approximately 1.84, and for TM_{12} is approximately 3.05.

The annular ring antenna with a mean radius of 3.97 mm was simulated based on the geometric constraint. The fundamental mode TM_{11} produces resonance around 7 GHz as observed from the reflection coefficient response plotted in Fig. 1a. The resonant frequency is also consistent with the theoretical value of 6.93 GHz calculated with the relation (1). The impedance matching is not adequate, and the minimum reflection coefficient is around -14 dB. The desired resonant frequency is 2.45 GHz; thus, modification is necessary to reduce the resonant frequency of the fundamental mode. For this purpose, another concentric ring was introduced within the principal ring to enhance the effective radius and consequently reduce the resonant frequency of the fundamental mode. The resonant frequency of the fundamental TM_{11} mode is noticeable around 2.45 GHz with inadequate impedance matching, as shown in Fig. 1b. Also, it can be observed that a higher-order mode is also resonating around 5.8 GHz.

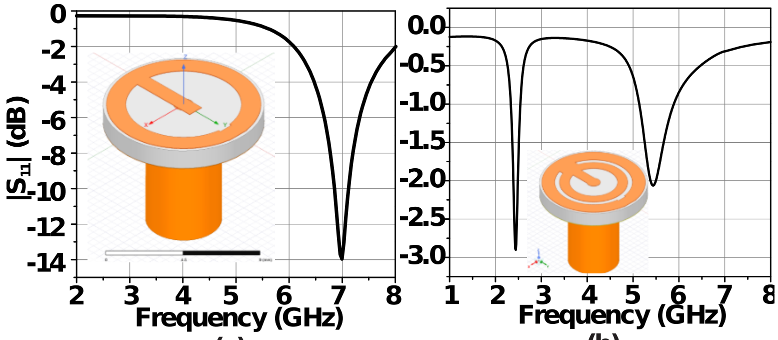

(a) (b)

Figure 1. Reflection coefficient of single and double annular ring geometry.

A solid ground plane was used for the aforementioned simulations. In order to tune the resonant frequency and match the impedance, the ground plane was made defective by adding a circular slot that resembles a complementary split ring. This defective ground plane modifies the boundary conditions and current mapping, resulting in impedance optimization. The fundamental mode has been matched with the help of the defective ground. The higher-order mode resonating around 5.8 GHz is still weak. The reflection coefficient response with the defective ground is shown in Fig. 2. The modified geometry, as well as the surface current plot, is presented alongside the reflection coefficient in the figure.

For radial order identification, it can be concluded that the design of the ring is electrically narrow in the radial direction and therefore supports only the fundamental radial order n = 1, which is consistent with a single radial field maximum in the underlying cavity. To identify the azimuthal order, the surface current distribution vector plot from Fig. 2 reveals the angular phase progression around the ring. It can be observed that the current flows predominantly in one direction around the ring and completes a single complete field cycle by undergoing two phase reversals at φ = 90° (+ y axis) and at φ = 270° (- y axis), with no intermediate reversal. This behaviour shows that the azimuthal index is also 1, thus the fundamental mode is identified as TM_{11}. However, it was also observed that some H field vectors have non-transverse field components, so the resonating mode is not a pure TM mode. This behaviour is common owing to the defective ground plane underneath.

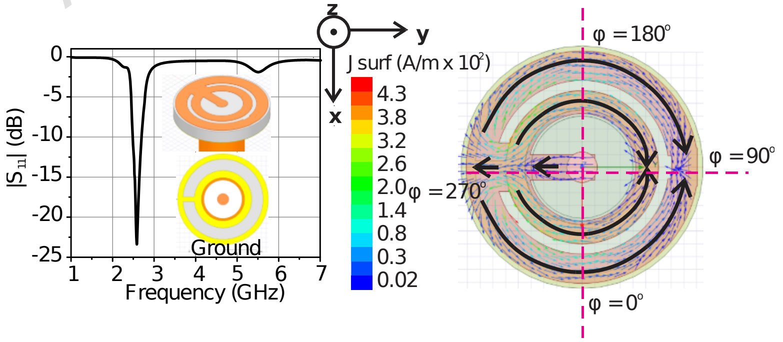

Figure 2. Reflection coefficient of the optimized dual annular ring antenna with defected ground and the surface current vector plot at 2.45 GHz

The higher-order mode, which appears at 5.8 GHz, has a weak resonance, and since there is no other resonance between the fundamental mode and this mode, it is concluded that the higher-order mode is TM_{12}. This mode can be tuned for the 5.8 GHz band. A dual feed arrangement is necessary to excite the TM_{12} mode because it is an even mode with dual azimuthal variations. The feeding microstrip is extended to the right to link the ring and initiate the even mode in order to achieve the dual excitation.

The simulated reflection coefficient response of the modified feed geometry is shown in Fig. 3. It can be seen that the second mode is now resonating with adequate impedance matching.

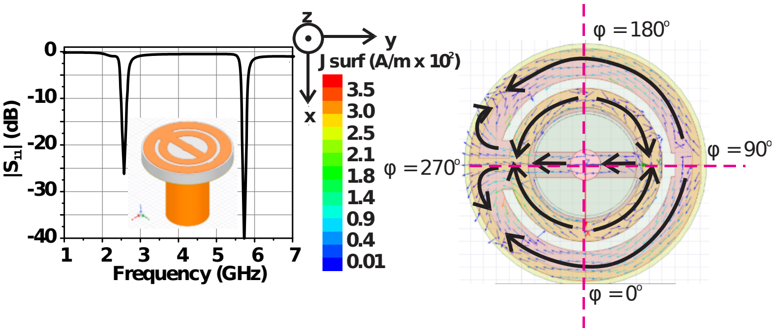

Figure 3 Reflection coefficient of dual-band annular ring antenna, surface current vector plot at 5.8 GHz

To identify the order of the higher mode surface current vector plot is overlaid with directional arrows (Fig. 3). The electrically narrow ring corresponds to a single radial peak, hence the radial order ‘n’ is still 1. Likewise, for the azimuthal variation, the current vectors undergo four phase reversal points along the circumference. For clear observation, the inner ring can be examined, and phase reversal can be seen at φ = 0° (+ x axis), φ = 90° (+ y axis), φ = 180° (-x axis), and φ = 270° (-y axis). These four phase reversals correspond to two full wave variations (two maxima and two minima); therefore, azimuthal order ‘m’ is 2, and the mode is TM_{12}. The dual ring geometry acts as a radial extension only and does not alter the modal nature, so the azimuthal variation can be examined on either ring.
The optimized geometry for the single-band antenna is presented in Fig. 4. The parameters are shown for the fundamental mode (TM_{11}) excitation, whereas for dual-mode excitation, the feeding strip is extended on the right side to connect the inner ring. The antenna itself is 1.27 mm thick, and the feeding is carried out through a coaxial connector with impedance of 50 Ohms. A small notch (tw3 × tw4) is introduced on the larger ring for impedance matching only.

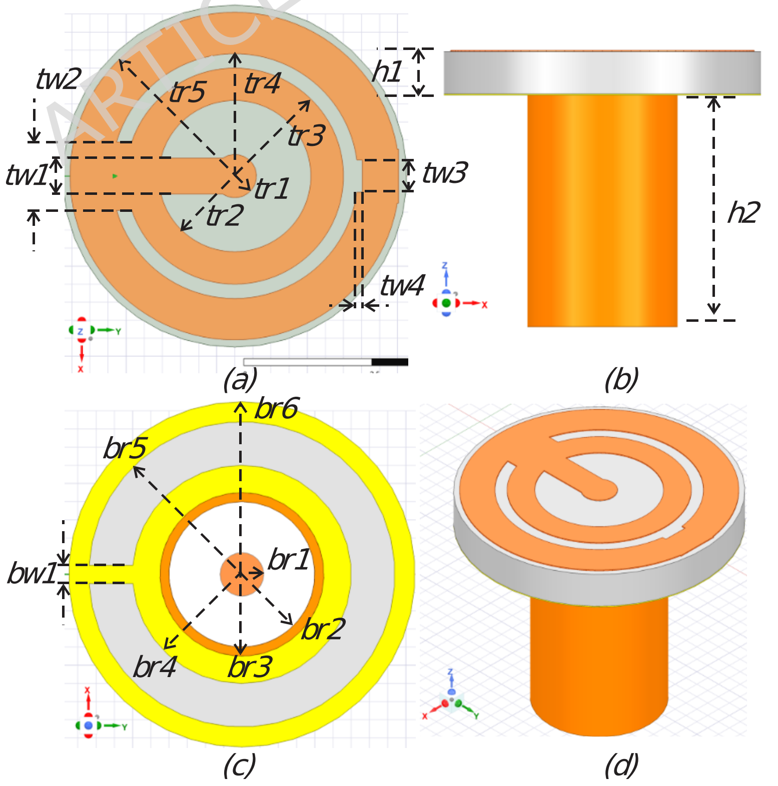

Figure 4 Optimized antenna geometry (a) Top view (b) side view (c) Bottom view (d) perspective view, the values are ; tr1 = 0.6 mm, tr2 = 2.1 mm, tr3 = 3 mm, tr4 = 3.4 mm, tr5 = 4.54, h1 = 1.27 mm, h2 = 6 mm, tw1 = 1 mm, tw2 = 1.9 mm, tw3 = 0.9 mm, tw4 = 0.15 mm, br1 = 0.6 mm, br3 = 2.25, br4= 3 mm, br5 = 4.2 mm, br6 = 4.75 mm, bw1 = 0.5 mm, br2 = 2 mm

The realized gain radiation patterns of E plane and H plane are presented in Fig. 5. These radiation patterns were simulated in free space, and the antenna offers a realized gain of -0.46 dBi for the fundamental mode and -0.69 dBi for the second mode. Since the proposed antenna is electrically small and the radiating conductor is patterned, the gain values for such small antennas are commonly negative.

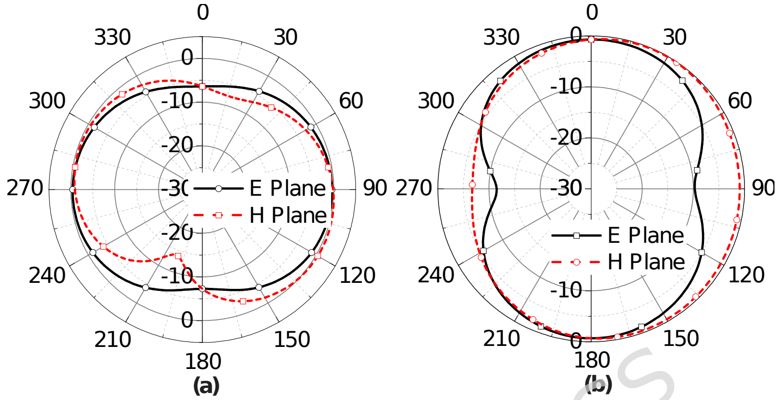

Figure 5. Simulated realized gain plot of dual-band annular ring antenna at (a) 2.45 GHz, (b) 5.8 GHz.

Biocompatibility and Specific Absorption Rate

The proposed antenna will be used within the ingestible capsule for endoscopic applications. It is therefore imperative to ensure the biocompatibility with the human body. The most common material used for ingestible applications is polytetrafluoroethylene (PTFE), which is also referred to as Teflon. Teflon has a high level of inertness with a relative permittivity of 2.1 and a dielectric loss tangent of 0.0004; thus, it is very popular as a biocompatible material [23]. The outer diameter of the capsule is 12 mm, and inner diameter is 10 mm, and the length is 21 mm. A coaxial connector of 6 mm was used to feed the antenna for simulation purposes; however, in an actual application, the coaxial connector would be replaced with a base board RF front-end. Thus, the proposed antenna only engages 1.27 mm of the capsule length and leaves the rest for associated circuitry, including the camera and sensors.
SAR analysis of the antenna is mandatory to ensure its safe operation; thus, a cylindrical single-layer phantom of a diameter of 120 mm was used to embed the capsule, as shown in Fig. 6. The relative permittivity ε_r of the intestine is 54.5, and the conductivity σ is 3.13 S/m for 2.45 GHz [24]. The SAR evaluation was computed in HFSS Modal solver in the frequency domain. The excitation was normalized to 1 W of power, and the resulting peak SAR values were later scaled to obtain the maximum allowable transmit power in accordance with IEEE C95.1-2009 10 g SAR limit. HFSS uses an adaptive finite element method meshing mechanism. The adaptive meshing was performed inside the entire phantom, along with the antenna and the surrounding air space. The mesh refinement process continued till the 10 g SAR values changed by less than 2 % between consecutive passes, which is the standard refinement criterion. The final mesh incorporated fine local refinement around all high field gradient regions, ensuring the SAR stability and repeatability. SAR is computed by automatically subdividing the phantom into small 3D voxels, and in this case, the average voxel resolution was set to 1.0 mm, which is consistent with HFSS default biological tissue models. Reducing the resolution any further shows little change in the SAR values.

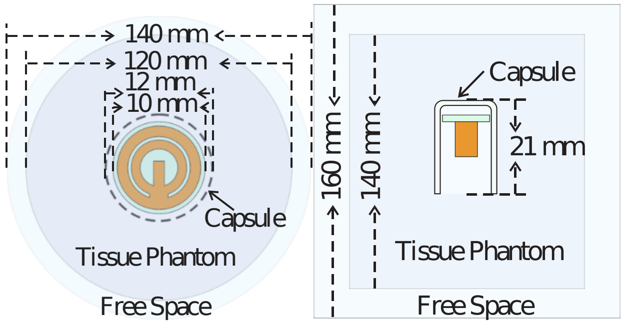

Figure 6. Simulation setup for SAR Calculation; Top view and side view

The average SAR plot for 10 g of mass for 2.45 GHz is shown in Fig. 7a. The maximum SAR of 21.52 W/kg has been observed. The maximum safe value allowed according to IEEE C95.1 and ECC standards is 2 W/g for 10 g of mass [25, 26]. The power level of the antenna should be reduced to ensure safe radiation exposure. The maximum allowed power, to ensure the safe SAR limit, is calculated to be 93 mW for the 2.45 GHz band, according to (3) [1].

$$P_{max} = P_{In} \times \left(\frac{SAR_{Limit}}{SAR_{achieved}}\right) \qquad (3)$$

Where:

Pmax is the maximum allowed power to be fed to the antenna to ensure the SAR remains in the prescribed limit

Pin is the power input to the antenna to calculate the SAR. It is kept at 1W

$SAR_{achieved}$ is the SAR calculated at the input power *Pin*

SAR_{limit} is the maximum allowed SAR as per the standard followed.

The dielectric properties change with frequency; the phantom was assigned revised values for the 5.8 GHz band. The relative permittivity ε_r is 48.7 and the conductivity σ is 6.75 S/m. SAR plot for 10 g of mass with revised values for 5.8 GHz is presented in Fig. 7b. The SAR values peak at 24.7 W/kg. Although the relative permittivity reduces, the conductivity, on the other hand, increased from 3.13 S/m at 2.45 GHz to 6.75 S/m at 5.8 GHz. There are other factors also involved, like penetration depth, that play a role in SAR. The power of 1 W was assigned to the port to generate the SAR plot, and the maximum allowed power to ensure SAR compliance is 81 mW for 5.8 GHz according to (3).
Although the maximum safe transmit power is reduced to 93 mW and 81 mW for lower and higher bands to comply with the SAR limit of 2 W/kg, practical operation would need lower power and lower duty cycle, particularly for the 5.8 GHz band. Since the time-averaged SAR is proportional to both input power and duty cycle, by switching the 5.8 GHz band ON only when transmitting images, we can keep the average exposure significantly below the worst-case limits. The higher power of 93 mW at a lower frequency improves the link robustness and allows using lower data rates to tolerate higher path loss. Additionally, the ring geometry of the antenna spreads current circumferentially, avoiding strong localized current concentrations that typically lead towards SAR hotspots, so in this case, the SAR is uniformly distributed without hotspots, thus leading to better compliance.

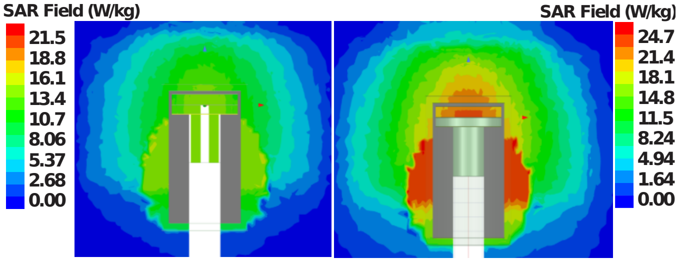

(a) (b)

Figure 7. SAR map of a capsule embedded inside the small intestine at (a) 2.45 GHz, (b), 5.8 GHz.

The simulated reflection coefficient of the antenna while embedded inside the intestine phantom is presented in Fig. 8. The dominant electromagnetic boundary experienced by the antenna is governed by the air and PTFE, which remains unchanged after the tissue loading also the reactive energy storage is dominated by the inductive currents along the ring rather than the fringing fields, thus the embedded antenna inside the phantom does not undergo a major resonant shift.

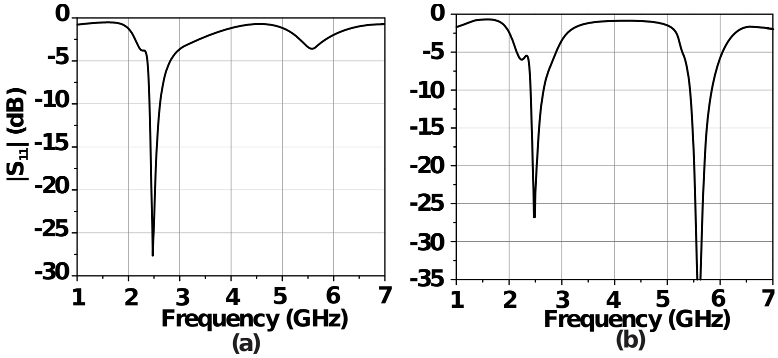

Figure 8. Reflection coefficient of the antenna embedded in the intestine phantom (a) single band antenna (b) dual band antenna

The simulated radiation pattern of the proposed ring antenna, while embedded inside the intestine, is presented in Fig. 9. The realized gain for the lower frequency band is reduced to - 17.66 dBi, and for the upper band, the maximum realized gain is - 19.34 dBi. The gain reduction is caused by heavy loading of a lossy and high-permittivity phantom, and significant power is absorbed very close to the antenna. This phenomenon is common for ingestible antennas. Radiation efficiency also reduced from 60.7 % in free space to 56.65 % in the phantom for the lower band and from 59.3 % in free space to 42.73 % in the phantom for the higher band.

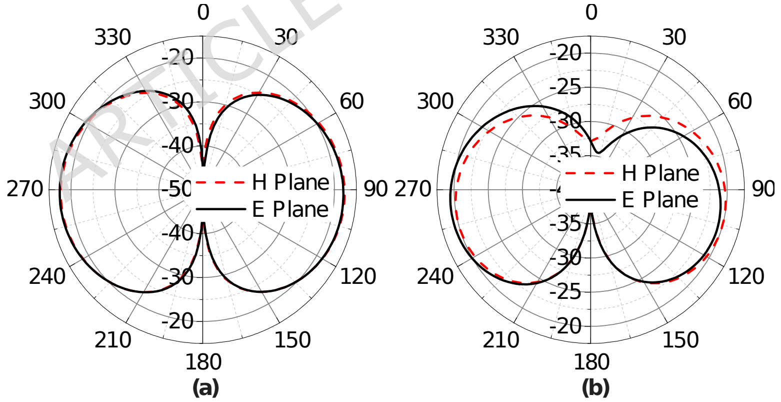

Figure 9. Simulated realized gain plot for capsule antenna embedded in phantom at (a) 2.45 GHz, (b) 5.8 GHz.

Electronic switching of the upper band

The upper frequency band, resonating around 5.8 GHz, offers the capability of being electronically switched ON and OFF. The antenna is designed such that when the feeding transmission line is connected across the inner ring to both edges, both the upper and lower bands are generated. Conversely, connecting the line only to the left edge of the ring excites the lower band only. To enable this functionality, an RF switching element, such as a PIN diode, can be incorporated to electronically connect or disconnect the feeding line segment to the right edge of the inner ring. The proposed configuration was evaluated through simulations using an equivalent lumped RLC model of the PIN diode for its ON and OFF states. Also, a DC block capacitor of 10 pF was added in series to the PIN diode to avoid a DC short when the diode is in the forward bias state. The simulator model is shown in Fig. 10. The proposed antenna is electrically small; thus, the signal leakage towards the biasing circuitry is a potential challenge. Therefore, two inductors of 22 nH were added to the two biasing points of the pin diode. The inductors are working as RF chokes to avoid signal leakage. The values of capacitors and inductors were calculated from the reactance relations.

The pin diode used for testing was BAR6302V (Infineon Technologies). The equivalent circuit used to simulate the lumped component for the ON and OFF states of the diode is also shown in Fig. 10.

The simulations were conducted with both states of the PIN diode to assess the performance of the dual-band antenna and higher band switching functionality. The reflection coefficient response is also presented in Fig. 10.

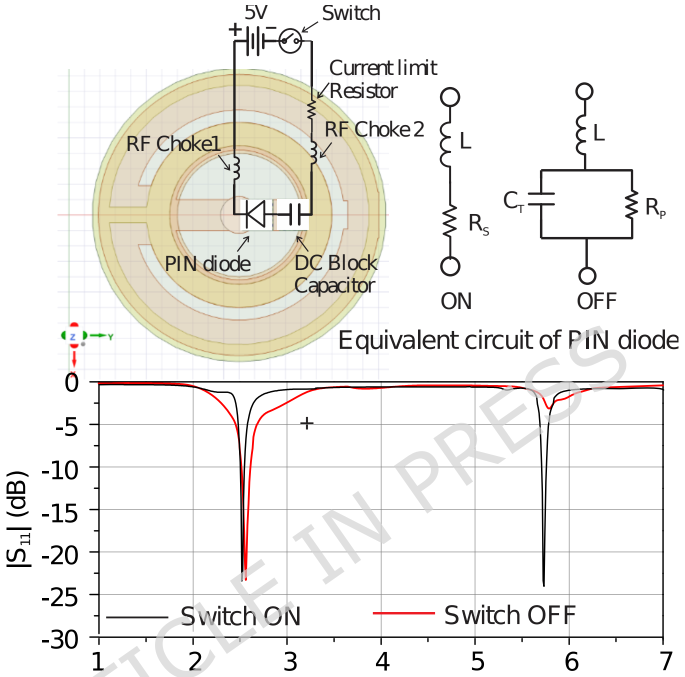

Figure 10. Simulation model for switchable dual-band antenna with lumped components. The equivalent schematic values for the lumped components are L = 0.6 nH, R_S = 1Ω, C_T = 0.3 pF, R_P = 5kΩ

It can be observed from the reflection coefficient that in the OFF state, the extended feeding line is disconnected from the right edge of the ring. The junction capacitor C_T is critical for high-frequency switching at 5.8 GHz; this capacitance offers reactance of 212 Ohms, which is very high to allow the RF signal to leak through. Therefore, in the OFF state, the antenna behaves as a single-band antenna with weak excitation at 5.8 GHz. While in the ON state, it allows the RF signal to pass through without much attenuation, thanks to the low series resistance. The antenna is operating in dual-band mode as desired.

Fabrication and testing

Three versions of the proposed antenna were fabricated. The substrate used was Rogers 3010 high-frequency laminate with a thickness of 1.27 mm. The antenna is hermetically enclosed in a PTFE capsule, so it is not in direct contact with tissues. A strict biocompatibility demand only applies to the covering capsule, but not to this antenna material; therefore, other substrates like alumina and high permittivity ceramics can also be used. One variant was a single-band antenna where the feeding line was connected to the left side only; the antenna offers a single-band response at 2.45 GHz. The other variant was the dual feed antenna, where the feedline was extended to the right side as well, exciting the second mode for the 5.8 GHz band. The third variant of antenna was with a PIN diode to switch the band electronically. The antennas were fabricated using an LPKF S103 milling machine. The SMA connector was used to feed the antennas.

A. Single-band antenna results

The single-band antenna resonating at 2.45 GHz is shown in Fig. 11. It can be observed that the single-band antenna is operating as intended. The resonant frequency shows a broader band coverage as compared to the simulation. The ground plane is small; therefore, there is a possibility of common-mode current generation (sheath current), and to ensure isolation, a ferrite bead was fixed on the measurement cable to avoid current leakage. Overall, the simulated and measured responses are in good agreement

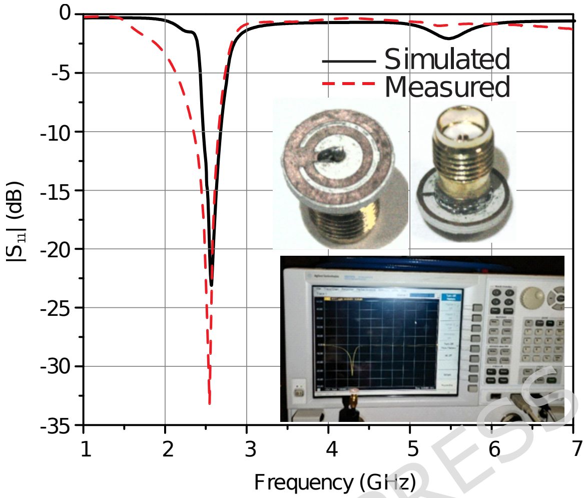

Figure 11. Simulated and measured reflection coefficient of the single-band antenna in free space

The antenna was tested in free space with the N5242A PNA-X network Analyzer. The radiation pattern of the antenna was measured in free space in an anechoic chamber; A comparison of the simulated and measured radiation patterns is shown in Fig. 12. The realized gain values are consistent with the simulation; a slight distortion is observed in the measured results. The maximum gain measured in the E plane is 0.1 dBi. The H plane is also following the simulated response with a certain distortion. The gain of the H plane is also consistent with the simulated results. The maximum gain in the H plane is 0.2 dBi.

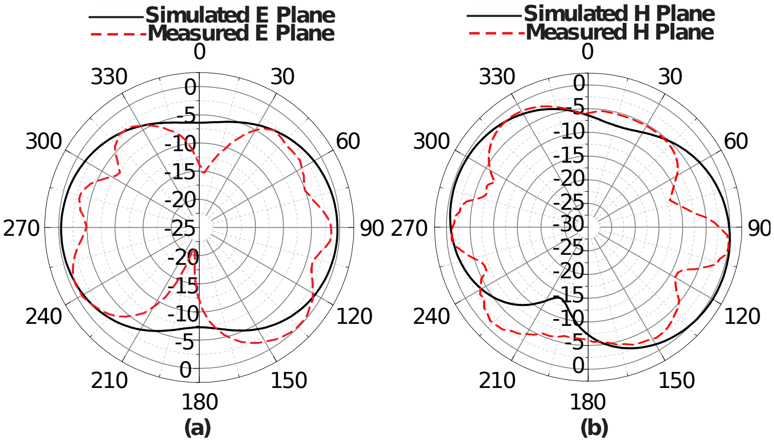

Figure 12 Simulated and measured radiation patterns in free space at 2.45 GHz (a) E Plane (b) H Plane.

The small intestine can be mimicked using minced chicken breast [17, 27]. The relative permittivity ε_r at 2.45 GHz for a chicken breast is 53.2, and the conductivity σ is 2.76, whereas for a small intestine, the relative permittivity is ε_r 54.5 and the conductivity σ is 3.13. These values are close enough to be considered as a reasonable substitute for the small intestines.

The minced meat was placed in a plastic container of diameter 120 mm and depth 70 mm, and it was pressed firmly to ensure no air bubbles were trapped. The antenna was embedded inside the PTFE capsule. The setup is shown in Fig. 13.

The simulated and measured reflection coefficient of the single-band antenna inside the minced meat is shown in Fig. 14. The measured results are in agreement with the simulated response. The principal resonant frequency at 2.45 GHz has a maximum reflection coefficient of -18 dB.

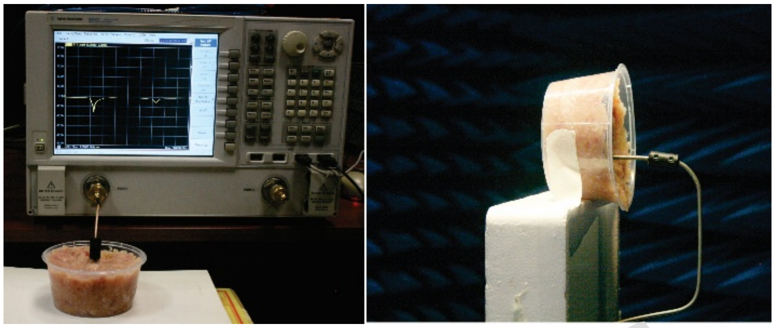

Figure 13. Measurement setup of antenna embedded inside chicken meat (a) Reflection coefficient (b) Radiation pattern

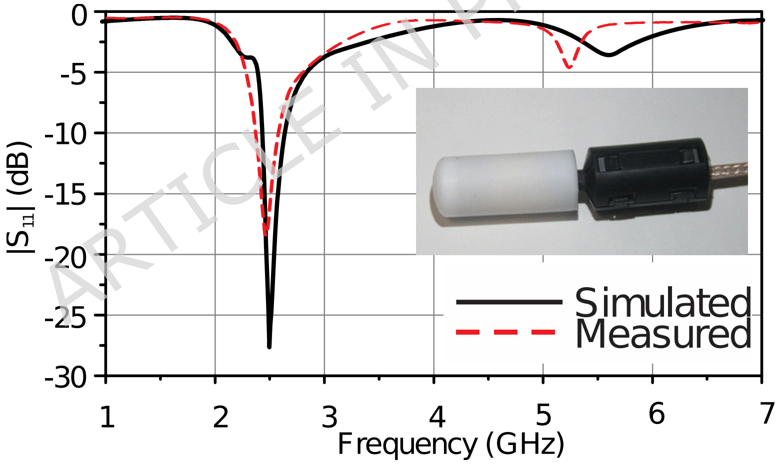

Figure 14 Simulated and measured reflection coefficient of the single-band antenna embedded in minced meat.

The radiation pattern was also measured while the antenna was kept inside the mined meat. The measured radiation pattern of both planes is compared with the simulated responses, as shown in Fig. 15. The results of the radiation patterns for both planes are similar to the simulated responses. The E-plane radiation pattern is consistent with the simulated results, and the radiation pattern is omnidirectional. In the H plane, the response follows the profile of simulations as well. The maximum measured realized gain in the E plane is -18.5 dBi, and for the H plane, the maximum measured realized gain is -17.3 dBi.

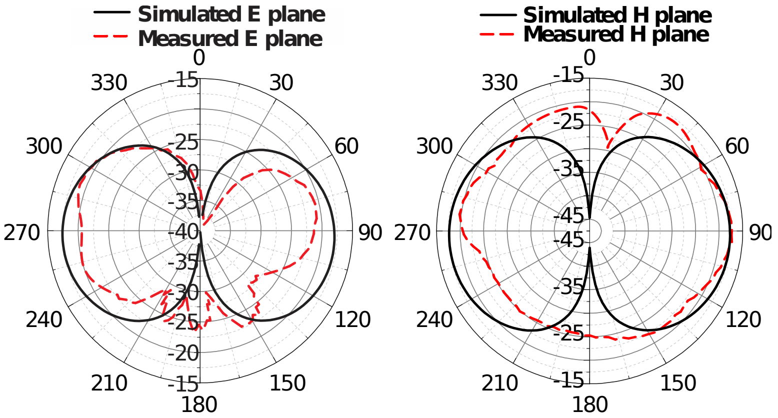

(a) (b)

Figure 15 Simulated and measured radiation pattern of single-band antenna within the minced meat at 2.45 GHz (a) E plane (b) H plane.

B. Dual-band antenna results

The dual-band antenna was also fabricated similarly to the single-band antenna. The feed line for the dual-band antenna is connected to both the left and right edges of the ring to excite dual modes. The dual-band antenna was first measured for its resonance response in free space using the VNA. The comparison of simulated and measured reflection coefficient in free space is presented in Fig. 16. The measured response is very much in agreement with the simulated reflection coefficient. The upper band has a slightly enhanced bandwidth; the lower band is consistent. Both frequency bands are slightly shifted towards the lower frequencies.

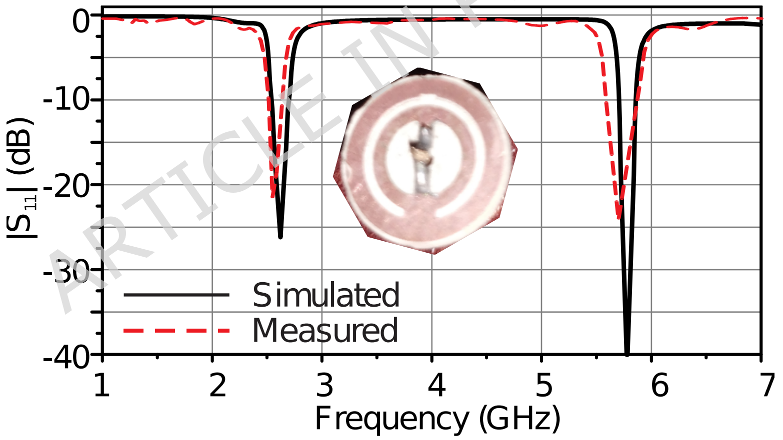

Figure 16 Simulated and measured reflection coefficient of the dual-band antenna in free space

The radiation pattern of the dual-band antenna was measured in free space and presented in Fig. 17. Both E and H planes of the dual-band antenna are consistent with the simulated response. The maximum measured realized gain for the E plane radiation pattern is -2.3 dBi, and for the H plane, -1.2 dBi.

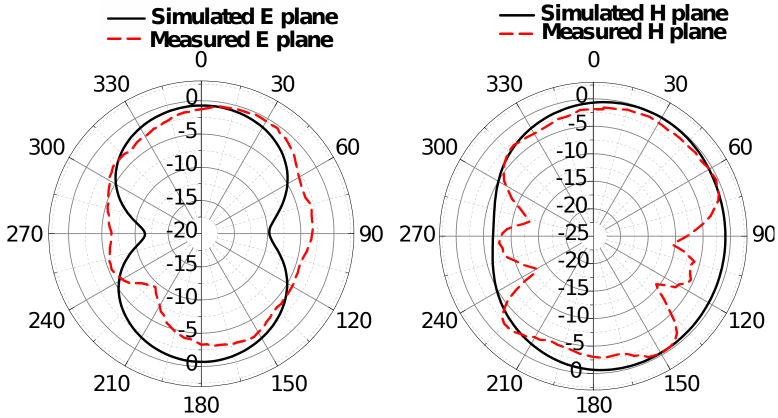

(a) (b)

Figure 17 Simulated and measured radiation pattern of dual-band antenna at 5.8 GHz in free space.

The permittivity of the small intestine at 5.8 GHz is 48.7, and the conductivity is 6.75. The relative permittivity of chicken breast at 5.8 GHz is approximately 47, and the conductivity is 6.44 [27]. These values are very close to the actual values of the small intestine at this frequency. The dual-band antenna was embedded inside the minced chicken meat to measure the reflection coefficient. The comparison of simulated and measured reflection coefficient is presented in Fig. 18. The dual frequency band response is prominent; a slight shift is attributed to the possible variation of the minced meat permittivity in comparison with the simulations. Antenna offers -10 dB bandwidth of 20.8 % from 2.32 GHz to 2.86 GHz for the lower band and 6.7 % from 5.48 GHz to 5.86 GHz for the higher band for in-vitro measurements.

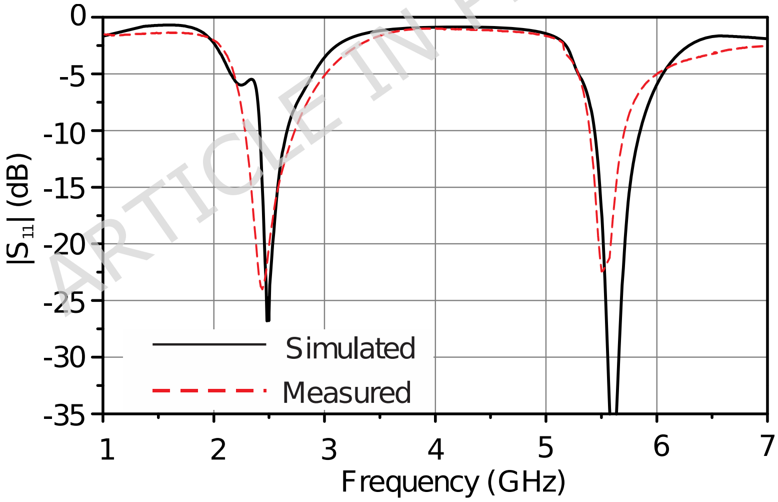

Figure 18 Simulated and measured reflection coefficient of the dual dual-band antenna embedded in the minced meat.

The Radiation pattern was also measured while the dual-band antenna was embedded inside the minced meat; the radiation patterns are compared with the simulated ones in Fig. 19. The radiation pattern in the H plane is in good agreement with the simulated response; however, the radiation pattern in the E plane is slightly off from the simulated response between θ = 260° to 330°. The maximum realized gain measured in the E plane is -18 dBi, whereas in the H plane, the maximum realized gain measured is -20 dBi.

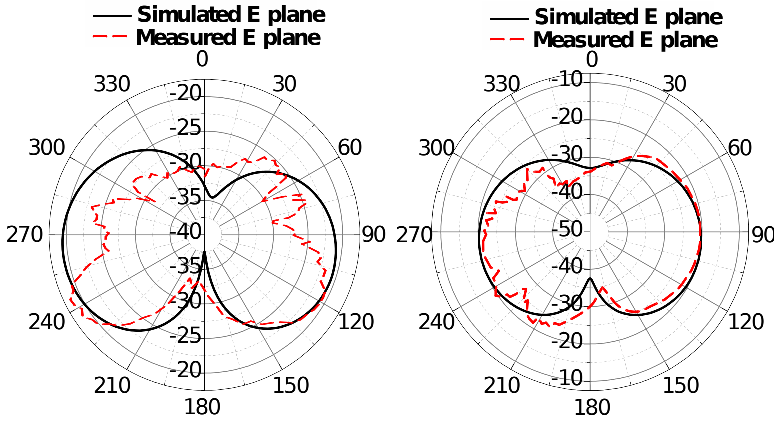

(a) (b)

Figure 19 Simulated and measured radiation pattern of dual-band antenna inside minced meat at 5.8 GHz.

C. Electronically switchable dual-band antenna

Finally, the third variant, which is electrically switchable, was also fabricated and measured. The PIN diode, two RF chokes of 22 nH each at the DC line, and an inline DC block capacitor of 10 pF were used. The fabricated antenna with lumped components is shown in Fig. 20. The antenna was only tested for S parameters in free space to prove the concept. A series resistance was used with the DC power supply to regulate the current flow. The diode was switched at 5 V, and the series resistance of 250 Ohms was added to control the current.

Figure 20 Fabricated switchable antenna with lumped components and measurement setup.

The measured results of the switchable antenna are compared with the simulated results in both ON and OFF states. The comparison shown in Fig. 21 illustrates the behaviour of the antenna. The measured results are in good agreement with the simulated results. The resonant frequency is measured at 2.5 GHz with slightly enhanced bandwidth as compared to simulations. The response in the ON state, on the other hand, shows a reduction in the bandwidth as well as a slight shift in the lower band frequency. These effects are mainly caused by parasitic inductance and capacitance of the PIN diode, and biasing inductors also affect the reflection coefficient as the antenna near field is interacting with the DC feed lines.

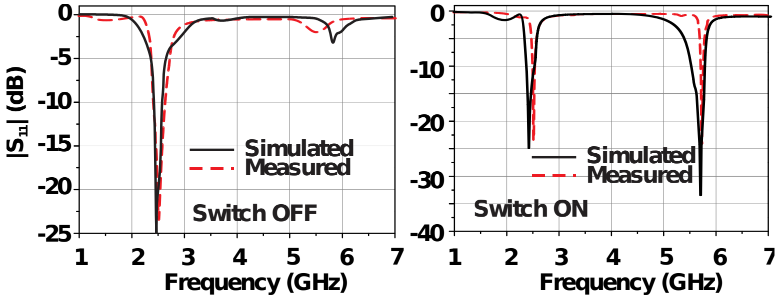

(a) (b)

Figure 21 Simulated and measured reflection coefficient of electronically switchable antenna.

The switchable antenna was tested in ON and OFF states for free space measurements; the enclosure in the PTFE capsule is expected not to alter the behaviour due to consistent boundary conditions. Since it was a very delicate design so it was not possible to enclose it in the capsule and carry out the in vitro testing in minced meat. It was also not possible to arrange a DC biasing supply in the anechoic chamber; thus, the radiation patterns were not measured. However, the study of fixed single and dual band variants corroborates the switching functionality of this antenna.

Link margin analysis

Reliable wireless communication between the ingestible capsule and an external Wi-Fi access point requires sufficient link margin under realistic indoor propagation conditions. To assess the long-range connectivity of the proposed dual-band antenna, a detailed link budget analysis was performed, similar to the prior published research [15, 28, 29]. The link budget incorporates SAR-limited transmit power, measured realized gains inside tissue-equivalent material, free-space propagation from the body to the Wi-Fi access point, receiver sensitivity of the Wi-Fi access point, and an additional margin for body shielding and indoor fading. The matrix used to present the link reliability is called link margin, which quantifies how much stronger the received signal is compared to the minimum required sensitivity of the receiver. A positive link margin of 10 dB or more indicates a reliable link. It is calculated as (4)

$$\mathrm{LM}(d) = P_{RX}(d) - S_{RX} \tag{4}$$

Where:

$\mathrm{LM}(d)$ is the link margin at a distance d

$P_{RX}(d)$ is received power at the receiver with distance d

S_{RX} is receiver sensitivity

A. Receive power model

The received power at a distance d is given by the standard link budget relation (5) [30]

$$P_{RX}(d) = P_{TX} + G_{TX} + G_{RX} - PL_{FS}(d) \tag{5}$$

Where:

P_{TX} is the maximum transmitting power that is allowed while complying with the SAR regulation

G_{TX} is the capsule antenna realized gain measured in the minced meat phantom

G_{RX} is the gain of the Wi-Fi receiver antenna

$PL_{FS}(d)$ is the free space path loss given by (6)

$$PL_{FS}(d) = 20\log\left({}^{4\pi df}/_{c}\right) \tag{6}$$

B. Receiver sensitivity for the Wi-Fi access point

A conservative Wi-Fi link using BPSK ½ modulation, the receiver sensitivity depends on the noise floor, bandwidth, noise figure, and desired SNR. Following the standard practice [31] the receiver sensitivity is calculated using (7)

$$S_{RX} = N_o + 10\log(B) + NF + SNR \tag{7}$$

Where:

N_o is thermal noise power density computed as a product of Boltzmann constant (k) and Thermal temperature T,

$N_0 = kT,\ N_0 = (1.38 \times 10^{-23})(290)$

$N_0 = 4.0 \times 10^{-21}\ {}^{W}/_{Hz}$

$N_0 = -174\ {}^{dBm}/_{Hz}$

B is the bandwidth used for Wi-Fi physical

NF is the noise figure
SNR is the Signal-to-noise ratio for BPSL ½
All parameters used to calculate link margin are listed in Table I.

Table I: Parameters used for calculating the link margin

Parameter	Value
P_{TX} @ 2.45 GHz	19.7 dBm
P_{TX} @ 5.8 GHz	19.1 dBm
G_{TX} @ 2.45 GHz	-17.3 dBi
G_{TX} @ 5.8 GHz	-18.0 dBi
G_{RX}	2 dBi
N_0	174 dBm/Hz
B	20 MHz
SNR (½ BPSK)	10 dB
Shadowing	15 dB

The ideal link margin calculated according to (4) is 36.11 dB for 2.45 GHz and 27.32 dB for 5.8 GHz at a distance of 4 m. However, in realistic conditions, shadowing and fading occur due to body and capsule orientation; therefore 15 dB shadowing margin has been added to the link margin. The revised link margin is 21.11 dB and 12.32 dB for 2.45 GHz and 5.8 GHz, respectively. The computed link margin is plotted in Fig. 22 against distance for better understanding.

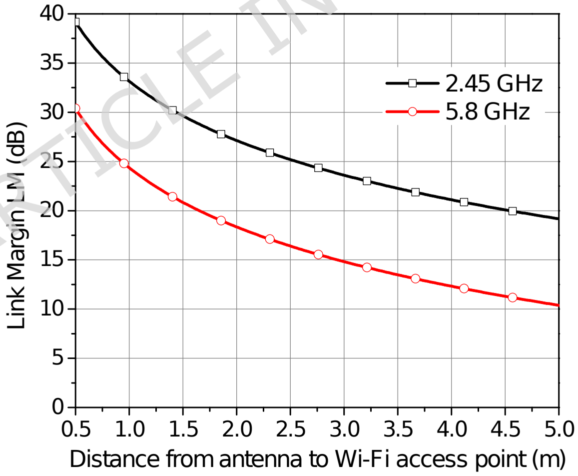

Figure 22 Calculated Link margin for the antenna at 2.45 GHz and 5.8 GHz.

A comprehensive comparison between the proposed antenna and previously reported designs from relevant literature is provided in Table II. All antennas included in the comparison are planar, capsule-based configurations designed for ingestible applications in abdominal endoscopy. It can be observed that the proposed band offers the best gain as well as the lowest SAR values. Also, the size of the proposed antenna is at par with the state of the art. Most importantly, none of the ingestible antenna designs offer electronic switching of a frequency band.

Table II: Comparison of the proposed antenna with relevant literature

Ref	Freq. GHz	Size (mm)	BW* (%)	Type	Gain (dBi)	SAR (W/kg)	SW*
[16]	915/2.45	6.5×6.5	13.6/6.28	Square	- 28.2/- 24.5	45/27.7	No
[32]	2.45	$\pi\times5^2$	6.5	CD	-31.9	137.9 (1g)	No
[17]	2.45	$\pi\times5^2$	3.9	Dual-layer CD	-26.4	530 (1g)	No
[18]	2.45	$\pi\times4.9^2$	6.1	CD	-24.6	45.5	No
[29]	2.45	$\pi\times4^2$	4.8	CD	-26.7	168 (1g)	No
[33]	2.45	2.6×3.0	6.15	Multi-layer square patch	-9.7	596 (1g)	No
[34]	2.45	$\pi\times3^2$	16.3	CD	-24.5	29.7	No
[19]	1.4/2.45	8.2×8.2	7.2/4.2	Square patch	- 29.4/ - 30.4	6.07	No
[15]	2.45	$\pi\times3^2$	44.02	CD	-20.8	30.2	No
This work	2.45/5.8	$\pi\times4.7^2$	20.8/6.7	CD	-17.3/-18	24.7	Yes

*CD: Circular Disk
*SW: Switchable
*BW: Bandwidth

Conclusion

The antenna design proposed in this work is a disc-shaped planar antenna that is based on dual annular ring topology. The antenna is proposed for an ingestible application for endoscopy of the small intestine. The antenna operates 2.45 GHz and 5.8 GHz ISM bands and both these bands are shared with Wi-Fi bands (2.400 GHz – 2.4835 GHz, 5.725 – 5.850 GHz), enabling it to directly communicate with the internet without the need for a gateway by incorporating Wi-Fi protocols at data link layer and transport layers, thus acting as an independent IoT node. The antenna covers less than 2 mm of the capsule length and thus leaving ample volume for camera installation and essentially a 360º field of view along the sides. The antenna has a compact diameter of 9.5 mm that fits easily in a 10 mm capsule made of PTFE. The antenna offers a dual-band response where the second band resonates at 5.8 GHz. The proposed antenna allows transmission powers of 93 mW and 81 mW for the lower and higher bands, respectively, which is better than the available ingestible antenna. A proof of concept for the band switching functionality has been presented using a PIN diode to turn ON and OFF the higher band. This allows the conservation of the on-board battery and reduces time-averaged SAR exposure; the upper band can be turned ON for short bursts of data, like images and video feed. The switching prototype with a discrete PIN diode and biasing wires is mechanically fragile and, therefore, was only characterized in terms of S parameters in free space. This limitation is only linked to this particular prototype; in future work, we shall address this limitation by a unified single PCB design that incorporates both the radiating and biasing networks.

Acknowledgments

The authors thank Dassault Systemes, France, for making CST Microwave Studio available. This work is partially supported by the Nobelium Joining Gdansk Tech Research Community DEC-17/2021/IDUB/I.1 and by the Icelandic Research Fund Grant 2410297.

Contribution statement

Conceptualization, N.G. (Nayab Gogosh) and S.Kh. (Sohail Khalid); methodology, N.G. and S.Kh.; data generation, N.G. and B.T.M (Bilal Tariq Malik).; investigation, N.G. and S.Kh.; prototyping and testing N.G. and M. Farhan Shafique (M.F.S) writing original draft preparation, N.G., and B.T.M.; writing review and editing, S.K. (Slawomir Koziel) and Stanislaw Szczepanski (S.S); visualization, B.T.M and S.K.; supervision, S.K. and S.Kh.; project administration, S.K and S.S.

Declaration of Competing Interest

The authors declare that they have no known competing financial interests or personal relationships that could have appeared to influence the work reported in this paper.

Data Availability

The datasets used and/or analyzed during the current study are available from the corresponding author on reasonable request.

References

[1] N. Gogosh, S. Khalid, B. T. Malik, and S. Koziel, "Artificial magnetic conductor backed dual-mode sectoral cylindrical DRA for off-body biomedical telemetry," *Scientific Reports,* vol. 15, no. 1, p. 31870, 2025.

[2] X. Yang *et al.*, "A substrate integrated adaptable wearable antenna for enhancing IOT communication," *IEEE Transactions on Components, Packaging and Manufacturing Technology,* 2025.

[3] R. K. Baudh, S. Sahu, M. S. Parihar, and V. D. Kumar, "A Novel Proximity Coupled Fed High Gain Circularly Polarized Wearable Antenna for On Body IoT-based Defense Applications," *IEEE Internet of Things Journal,* 2025.

[4] H. Rajagopalan and Y. Rahmat-Samii, "Wireless medical telemetry characterization for ingestible capsule antenna designs," *IEEE Antennas and Wireless Propagation Letters,* vol. 11, pp. 1679-1682, 2013.

[5] S. Fontana *et al.*, "State of the art on advancements in wireless capsule endoscopy telemetry: A systematic approach," *IEEE Open Journal of Antennas and Propagation,* vol. 5, no. 5, pp. 1282-1294, 2024.

[6] G. Iddan, G. Meron, A. Glukhovsky, and P. Swain, "Wireless capsule endoscopy," *Nature,* vol. 405, no. 6785, pp. 417-417, 2000.

[7] X.-Q. Zhu, Y.-X. Guo, and W. Wu, "Miniaturized dual-band and dual-polarized antenna for MBAN applications," *IEEE Transactions on Antennas and Propagation,* vol. 64, no. 7, pp. 2805-2814, 2016.

[8] S. S. Mosavinejad, P. Rezaei, A. A. Khazaei, and J. Shirazi, "A triple-band spiral-shaped antenna for high data rate fully passive implantable devices," *AEU-International Journal of Electronics and Communications,* vol. 159, p. 154474, 2023.

[9] T. Govindan *et al.*, "Design and analysis of a conformal MIMO ingestible bolus sensor antenna for wireless capsule endoscopy for animal husbandry," *IEEE Sensors Journal,* vol. 23, no. 22, pp. 28150-28158, 2023.

[10] Z. Bao, Y.-X. Guo, and R. Mittra, "Conformal capsule antenna with reconfigurable radiation pattern for robust communications," *IEEE Transactions on Antennas and Propagation,* vol. 66, no. 7, pp. 3354-3365, 2018.

[11] J. Wang, M. Leach, E. G. Lim, Z. Wang, R. Pei, and Y. Huang, "An implantable and conformal antenna for wireless capsule endoscopy," *IEEE Antennas and Wireless Propagation Letters,* vol. 17, no. 7, pp. 1153-1157, 2018.

[12] R. Gao, H. Sun, R. Ren, and H. Zhang, "Design of a Biomedical Antenna System for Wireless Communication of Ingestible Capsule Endoscope," *IEEE Antennas and Wireless Propagation Letters,* 2024.

[13] D. Nikolayev, A. K. Skrivervik, J. S. Ho, M. Zhadobov, and R. Sauleau, "Reconfigurable dual-band capsule-conformal antenna array for in-body bioelectronics," *IEEE Transactions on Antennas and Propagation,* vol. 70, no. 5, pp. 3749-3761, 2021.

[14] R. Das and H. Yoo, "A wideband circularly polarized conformal endoscopic antenna system for high-speed data transfer," *IEEE Transactions on Antennas and Propagation,* vol. 65, no. 6, pp. 2816-2826, 2017.

[15] A. Mohan and N. Kumar, "Compact wideband implantable antenna for wireless capsule endoscopy application in the 2.45 GHz ISM band," *Scientific Reports,* vol. 15, no. 1, p. 30644, 2025.

[16] S. Hayat, S. A. A. Shah, and H. Yoo, "Miniaturized dual-band circularly polarized implantable antenna for capsule endoscopic system," *IEEE Transactions on Antennas and Propagation,* vol. 69, no. 4, pp. 1885-1895, 2020.

[17] W. Cui, R. Liu, L. Wang, M. Wang, H. Zheng, and E. Li, "Design of wideband implantable antenna for wireless capsule endoscope system," *IEEE Antennas and Wireless Propagation Letters,* vol. 18, no. 12, pp. 2706-2710, 2019.

[18] L. Huang, H. Li, X. Ding, W. Shao, and S. Xiao, "A Compact Wideband Omnidirectional Circularly Polarized Implantable Antenna for Capsule Endoscopy System," *IEEE Antennas and Wireless Propagation Letters,* 2024.

[19] A. Alshammari, A. Iqbal, A. Basir, R. B. Simorangkir, and I. B. Mabrouk, "Ultraminiaturized dual-band implantable antenna for wireless capsule endoscopy," *IEEE Sensors Journal,* vol. 24, no. 9, pp. 15210-15218, 2024.

[20] A. Toktas, M. B. Bicer, A. Kayabasi, D. Ustun, A. Akdagli, and K. Kurt, "A novel and simple expression to accurately calculate the resonant frequency of annular-ring microstrip antennas," *International Journal of Microwave and Wireless Technologies,* vol. 7, no. 6, pp. 727-733, 2015.

[21] K. Lee and J. Dahele, "Theory and experiment on the annular-ring microstrip antenna," in *Annales des télécommunications*, 1985, vol. 40, no. 9: Springer, pp. 508-515.

[22] C. A. Balanis, *Antenna theory: analysis and design*. John wiley & sons, 2016.

[23] D. Fluoroproducts, "Teflon PTFE fluoropolymer resin: properties handbook," *DuPont Fluoroproducts: Wilmington, NC, USA,* 1996.

[24] I. I. Foundation. Tissue Properties Database V5.0 [Online] Available: https://itis.swiss/s/news-events/news/virtual-population/tissue-db-5-0

[25] *IEEE Standard for Safety Levels with Respect to Human Exposure to Radio Frequency Electromagnetic Fields, 3 kHz to 300 GHz*, I. S. C.-R. o. I. S. C95.1-1991), 2006.

[26] *IEEE Standard for Safety Levels With Respect to Human Exposure to Radio Frequency Electromagnetic*, C95.1-2019, I. S. C95.1-2019, 2019.

[27] S. Trabelsi, "Variation of the dielectric properties of chicken meat with frequency and temperature," *Journal of Food Measurement and characterization,* vol. 9, no. 3, pp. 299-304, 2015.

[28] M. S. Miah, A. N. Khan, C. Icheln, K. Haneda, and K.-I. Takizawa, "Antenna system design for improved wireless capsule endoscope links at 433 MHz," *IEEE Transactions on Antennas and Propagation,* vol. 67, no. 4, pp. 2687-2699, 2019.

[29] Z. Song, X. Xu, Y. Shi, and L. Wang, "Design of a compact circularly polarized implantable antenna for capsule endoscopy systems," *Sensors,* vol. 24, no. 12, p. 3960, 2024.

[30] D. M. Pozar, *Microwave and RF design of wireless systems*. John Wiley & Sons, 2000.

[31] T. S. Rappaport, *Wireless communications: Principles and practice, 2/E*. Pearson Education India, 2010.

[32] Y. Wang, B. Huang, and S. Yan, "A Dual-Polarized Meandered Ring-Slot Antenna for Wireless Capsule Endoscope Systems," *IEEE Antennas and Wireless Propagation Letters,* vol. 23, no. 6, pp. 1804-1808, 2024.

[33] G.-b. Wang, X.-w. Xuan, D.-l. Jiang, K. Li, and W. Wang, "A miniaturized implantable antenna sensor for wireless capsule endoscopy system," *AEU-International Journal of Electronics and Communications,* vol. 143, p. 154022, 2022.

[34] A. Alshammari *et al.*, "Compact in-band full-duplex implantable antenna for wireless capsule endoscopy," *IEEE Transactions on Antennas and Propagation,* 2024.